Comparison of Terahertz Transceiver Array Topologies in Multiobject Imaging

Yiran Cui, *Student Member, IEEE*, and Georgios C. Trichopoulos, *Member, IEEE*

***Abstract*—We investigate the effect of side lobe level (SLL) and multipath propagation in millimeter-wave(mmWave) and terahertz (THz) imaging systems for various transceiver array topologies. This work considers practical limitations in high-resolution active imaging systems and focuses on electrically large, planar antenna array topologies. As such, we investigate the imaging performance of sparse transmitting/receiving (Tx/Rx) array topologies that enable high angular/spatial resolution imaging with minimum hardware complexity. We show that 1) properly tapering the sparse array excitation can mitigate image clutter caused by high side lobes and 2) sparse arrays are more vulnerable to multipath reflections and clutter in dense scenes with highly reflective surfaces. We present both full-wave numerical analysis and laboratory experiments (250-300 GHz) to verify and compare the imaging array performance for several exemplary scenes.**

***Index Terms*—Terahertz imaging, sparse array, nonuniform amplitude, multipath reflection**

I. Introduction

In recent years, millimeter and terahertz (THz) waves (30 GHz – 10 THz) have become attractive in imaging applications due to the small wavelength, penetration into many common materials and thin biological tissues, and operation in low visibility conditions [1-3]. Additionally, THz waves are suitable for non-line-of-sight (NLoS) imaging due to their strong specular reflections from common rough surfaces [4-5].

Many early THz imaging techniques were developed based on optical components (e.g., lenses and mirrors) and mechanical raster scanning [6-7]. On the other hand, using antenna arrays is an alternative approach as it can achieve compact dimensions, low weight, and rapid image acquisition. Traditional antenna array theory requires that the spacing between the array elements must be less than $\lambda/2$, where λ is the wavelength of the highest operating frequency, to avoid any grating lobes in the array factor [8]. Nevertheless, for high-resolution imaging electrically large apertures are needed which can easily result in an unpractically large number of antenna elements. This poses engineering challenges due to the complex and lossy feeding networks [9].

Therefore, for active imaging systems, using sparse arrays is an attractive solution to reduce the number of elements while maintaining the attractive beamforming properties of the dense array counterparts. In sparse arrays, spacing between elements can be larger than $\lambda/2$. Although this will lead to grating lobes in the array factor, by properly designing the transmitting and receiving (Tx and Rx) arrays, these grating lobes can be removed in the two-way array factor (the product of the Tx and Rx array factors [10]). As such, sparse arrays can achieve similar two-way array factors to dense arrays while keeping much smaller total numbers of elements.

Using sparse arrays with uniform amplitudes on millimeter wave (mmWave) and THz imaging has been reported in [11-13]. Nevertheless, antenna arrays with nonuniform amplitudes can generate array factors with lower side lobes. Such capability is valuable in identifying objects with low reflectivity, thus increasing the system's dynamic range, and reducing clutter due to stray signals that originate from multiple reflections in the scene. For example, when an object with low reflectivity (weak scatterer, such as dielectric materials with relatively low permittivity) is located close to an object with high reflectivity (strong scatterer, such as metal), the reflection from the weak scatterer may be even lower than the side lobes of the strong scatterer. In this case, the weak scatterer will become invisible in the reconstructed image.

In this paper, for simplicity and without any loss of generality, we use linear antenna arrays and 2D images (range and cross-range) to show the imaging performance of multiple types of antenna arrays. Numerical and measurement results are presented in sections II and III, respectively.

II. Numerical Comparison of Dense and Sparse Imaging Arrays

To compare the performance of dense and sparse arrays, we numerically investigate several imaging scenarios. For simplicity and computational efficiency, we used a 2D EM simulator based the method of moments (MoM), namely WIPL-D 2D solver [14], to model a 2D imaging scenario (range and cross-range).

Several sparse array designing methods are introduced in [15]. Here, we intend to compare three array topologies, namely a traditional dense array with a half-wavelength spacing, a sparse array with uniform amplitudes, and another sparse array with nonuniform amplitudes. As such, using the approaches discussed in [15], we study three topologies:

a) *Dense array:* both the Tx and Rx arrays have 81 dense

This work was supported in part by the National Science Foundation under Grant CAREER ECCS-1847138.

The authors are with the School of Electrical, Computer and Energy Engineering, Arizona State University, Tempe, AZ 85281 USA (e-mail: ycui36@asu.edu; gtrichop@asu.edu).

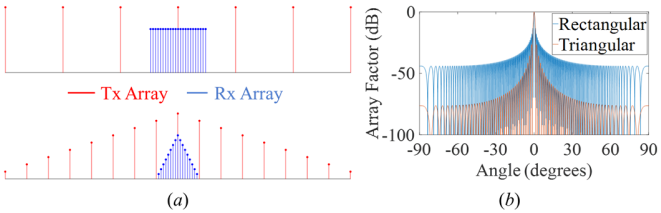

Fig. 1. Rectangular and triangular sparse array designs. (a) Arrangements of the array elements. (b) Normalized array factors of the effective apertures.

elements ($d_{Tx} = d_{Rx} = \lambda/2$) and uniform amplitudes.

b) *Rectangular excitation:* using the rectangular interpolation method (without tapering), the Tx is a sparse array with 7 elements and the Rx is a dense array with 23 elements ($d_{Tx} = 23 \times \lambda/2$, $d_{Rx} = \lambda/2$).

c) *Triangular excitation:* using the triangular interpolation method, the Tx and Rx arrays both have 17 elements and are sparse and dense, respectively ($d_{Tx} = 9 \times \lambda/2$, $d_{Rx} = \lambda/2$).

When the Tx and Rx arrays are colinear and centered at the same point, these three designs generate effective apertures with the same number of elements and spacing ($N = 161$, $d = \lambda/2$). The dense and triangular designs produce identical nonuniform effective apertures (thus they have the same array factors) whereas the rectangular design produces an effective aperture with uniform amplitudes. However, the dense design has a much higher total number of elements than the two sparse designs. The element arrangements and normalized two-way array factors of the two sparse designs (rectangular and triangular) are illustrated in Fig. 1. As expected, the rectangular interpolation leads to a narrower main lobe (the half-power bandwidth is approximately 0.3 degrees smaller) but higher side lobes (the first sidelobe and end-fire direction are approximately 13 and 32 dB larger, respectively).

In the following, we present simulation results using dense and sparse designs. The simulations are carried out in the frequency range of 250-300 GHz and both the transmitting and receiving antennas are linearly polarized and omnidirectional. Although in this work we use the image reconstruction method presented in [16], using other algorithms does not affect the comparison of different array topologies.

A. Side Lobe Comparison

First, we study a simple scenario with a 3 mm radius sphere (perfect conductor) placed 2.2 m in front of the imaging apertures to emulate a point scatterer. Thus, the acquired image represents the *impulse response* of the imaging system. Fig. 2 shows the obtained images using three different imaging array topologies for a 60-degree field of view (-30 to 30 degrees).

As expected, the dense and triangular designs generate indistinguishable images since they have identical effective apertures. Meanwhile, the rectangular design features much clearer traces in the cross-range direction due to higher side lobes, as shown in Fig. 1b. We use the target-to-clutter ratio (TCR) to measure the contrast of the target pixels with respect to the background [17]:

$$TCR = 20\log_{10}\left(\max(|f(i,j)|) \Big/ \frac{1}{N_C}\sum_{(i,j)\in C}|f(i,j)|\right) \quad (8)$$

where $f(i,j)$ represents the intensity of the (i,j) pixel, C represents the cluttered area, and N_C is the number of pixels in the cluttered area. Here, we select the cluttered area as bounded by 2 to 30 degrees with respect to the broadside in angle and -2 to 2 centimeters with respect to the brightest pixel in range (marked in white dashed lines in Fig. 2b and c). This region is large enough to provide a reliable estimate of the mean sidelobe and is safe to use since the object appears to be outside. As such, the TCR of the triangular and rectangular designs are approximately 68.3 and 50.7 dB, respectively. We note that the rectangular design has lower TCR due to higher sidelobes.

To investigate the effect of sidelobes on imaging performance in a more representative example, we carry out the following imaging scenario: a dielectric rode (ε_r=2) with a radius of 3 mm is placed close to a corner-shaped PEC rough surface, as shown in Fig. 3a. Thus, the roughness of the PEC object will create strong backscattering whereas the dielectric sphere has relatively weak backscattering. Fig. 3b and c compare the reconstructed images using the two sparse designs (rectangular and triangular). We notice that both images clearly show the shape of the corner, but it appears to be thinner in Fig. 3c due to the rectangular design having a narrower main beam, as shown in Fig. 1. However, the dielectric sphere is harder to identify in the case of rectangular design due to the strong traces in the cross-range direction generated by the rough PEC corner. In addition, in both images, there are noticeable bodies behind the corner. This is due to the strong specular reflection from the rough surface under THz frequencies, and the sphere appears to be mirrored behind the surface. This property can be exploited to implement THz NLoS imaging, as firstly shown in [4].

B. Imaging in the presence of multiple scattering

Although triangular tapering can achieve the same effective aperture as the dense design with much fewer elements, limitations occur when multiple objects are present in the scene. To illustrate that, we modify the scene shown in Fig. 2 (a single PEC sphere) and add another identical sphere such that the two spheres have the same distance to the aperture but are relatively far away from each other. In the image of the triangular design shown in Fig. 4b, the two spheres can also be reconstructed correctly, however there are observable artifacts. Again, we use the TCR to compare the artifacts with objects. Here, since each object corresponds to two artifacts near it, we use the lower object as an example and the cluttered areas are marked in white dashed lines in Fig. 4a and b (each sub-area features 4 cm and 6 degrees total ranges). As such, the dense and triangular topologies respectively have a TCR of 91.2 and 50.9 dB. The triangular topology leads to a smaller TCR due to the artifacts.

These artifacts are caused by the multiple reflections between the two spheres, as illustrated in Fig. 5. The triangular design includes a sparse Tx array, which generates multiple grating lobes. There are angles where the center of the main beams of the Tx and Rx array are not pointing toward any object. However, a grating lobe is pointing to one of the objects and, due to multiple reflections, the signal is received by the much wider Rx main lobe. At such angles, we observe artifacts that appear at a distance from the array equal to half of the distance

This article has been accepted for publication in IEEE Antennas and Wireless Propagation Letters. This is the author's version which has not been fully edited and content may change prior to final publication. Citation information: DOI 10.1109/LAWP.2023.3235206

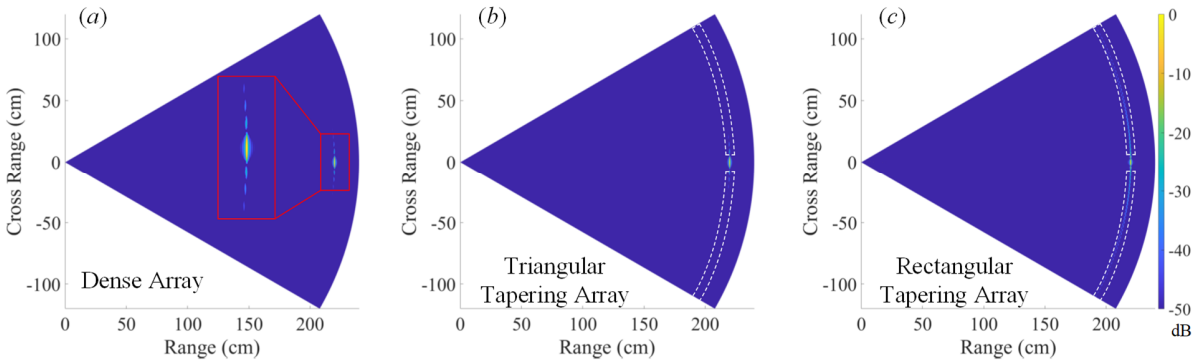

Fig. 2. Reconstructed images using different imaging array designs when a single PEC sphere is placed in front of the aperture. (*a*) Dense design. *Inset*: details of the target. (*b*) Triangular design. (*c*) Rectangular design.

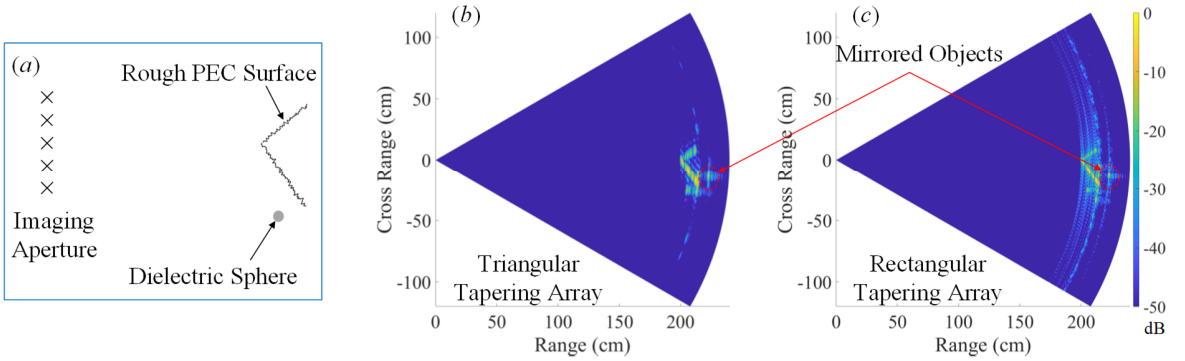

Fig. 3. A dielectric sphere and a rough PEC corner are placed in front of the aperture. (*a*) Simulation topology. (*b*) Reconstructed image using the triangular design. (*c*) Reconstructed image using the rectangular design.

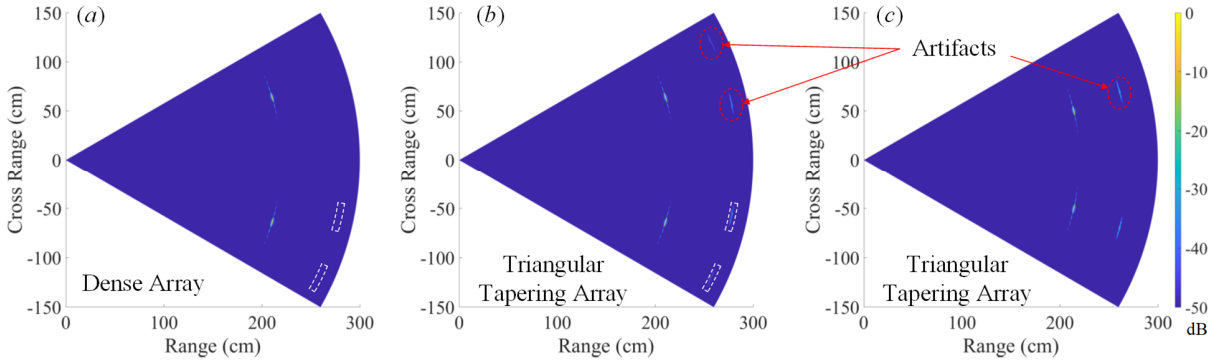

Fig. 4. Reconstructed images of two small PEC spheres. (*a*) Using the dense array. (*b*) and (c) Using the triangular tapering array for two different distances between the small spheres.

traveled by the multipath signal (green line in Fig. 5). This multiple reflection effect is similar to the *dihedral effect* [18]. Although in this imaging example we only include two objects, we can deduce that more objects would result in even more artifacts in the reconstructed images.

Furthermore, the locations of such artifacts are affected by the separation between two objects. For example, in Fig. 4c, the spheres are closer to each other, and the artifacts appear at different angles and distances with respect to the aperture. In the meantime, due to the different sphere locations, two artifacts appear near each object in Fig. 4b whereas only one in Fig. 4c. In contrast, dense arrays have identical single narrow and aligned beams for both Tx and Rx and reduce multipath clutter.

III. Imaging Experiments Using Dense and Sparse Arrays

Due to the lack of multielement antenna arrays in this frequency range, we implement a linear multistatic synthetic aperture imaging system to carry out various imaging examples. As such, two vector network analyzer (VNA) extenders (integrated with diagonal horn antennas), and two translation stages emulate the linear Tx and Rx arrays, as shown in Fig. 6. The Tx and Rx extenders are mounted on the respective translation stages (~ 1 μm precision) and are separated by a small distance on the vertical axis. The Tx extender moves to all the locations of Tx array elements one by one and transmits signals to the objects. Meanwhile, for each Tx location, the Rx extender moves to all the locations of Rx array elements in a

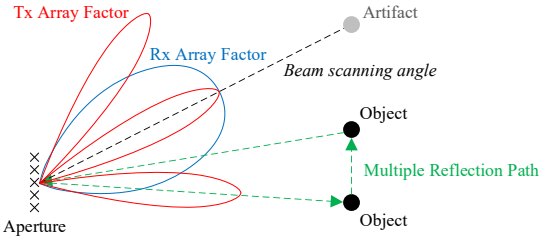

Fig. 5. Multiple reflection effect in a scene with more than one object.

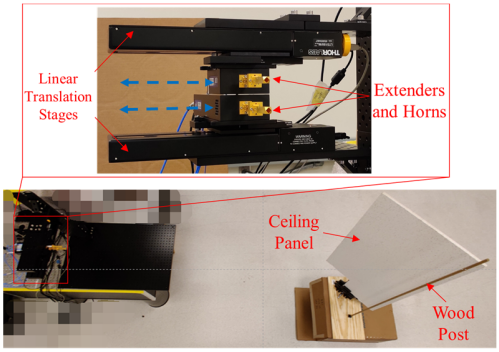

Fig. 6. Use VNA extenders and translation stages to emulate linear sparse arrays. A ceiling panel and a wood post are shown as the imaging objects.

similar way and coherently records the backscattered signals for both dense and sparse array topologies.

Similar to the numerical analysis, we set up three imaging scenarios that involve potential clutter. First, we use a metal post to demonstrate the side lobes of the two sparse array designs. As noticed in Fig. 7, the rectangular design generates higher side lobes.

Next, we form a scene with a weak and strong scatterer by placing a thin wooden post close to a ceiling panel, as shown in Fig. 6. As expected, since the sparse rectangular design leads to higher side lobes, the wooden post is barely distinguishable, as is observed in the reconstructed images in Fig. 8.

In the third measurement, we image two metal posts that are separately located. Fig. 9 compares the obtained images using the dense and triangular designs. We observe that there are artifacts in the image of the triangular design due to the multiple reflections between the posts. On the other hand, the dense design is immune to such problems.

IV. Conclusions

We studied the image aberrations of various transceiver topologies in active THz imaging systems. We found that triangular interpolation is an effective excitation when low SLL is needed in imaging with a sparse array. The simulation results show that the rectangular design exhibits much higher side lobes, which is detrimental in the presence of a weak scatterer next to much stronger ones. We also show that although sparse topologies offer valuable advantages in terms of lower system complexity while maintaining a same or even better SLL compared with dense arrays, it comes at the cost of imaging performance when multipath propagation is present. Therefore, using dense arrays is still the preferred approach in this case.

Future THz imaging applications may require the capability of identifying multiple objects in the scene with a relatively

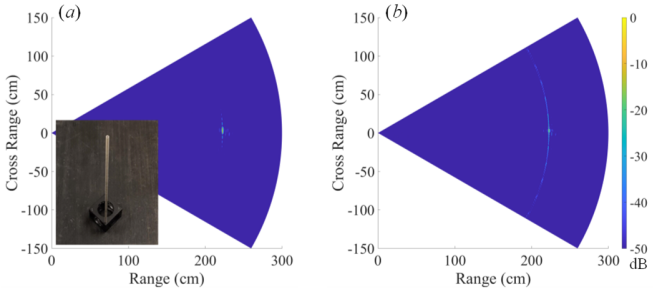

Fig. 7. Reconstructed images using different imaging array designs when a metal post is used as the imaging object. (*a*) Triangular design. (*b*) Rectangular design.

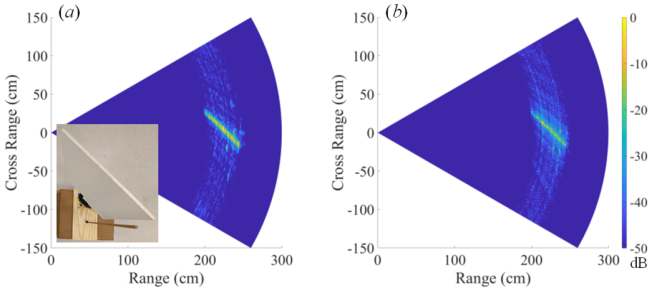

Fig. 8. Reconstructed images using different imaging array designs when a wood post and a ceiling panel are used as the imaging objects. (*a*) Triangular design. (*b*) Rectangular design.

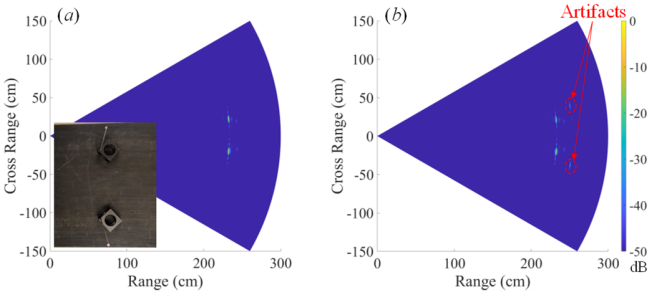

Fig. 9. Reconstructed images using different imaging array designs when two metal posts are used as the imaging objects. (*a*) Dense design. (*b*) Triangular design.

high resolution. Therefore, besides the advantages of sparse imaging topologies, the results presented here serve as a motivation for the use of dense arrays or other non-sparse topologies (e.g., reconfigurable lenses/reflective surfaces [19]) when maximum clutter mitigation is needed.

In both the imaging simulations and measurements, we do not account for the mutual coupling between antenna array elements. In the simulations we only compute the scattered fields, and the synthesized aperture used in the experiments does not involve mutual coupling since only one Tx/Rx antenna is present. However, in an actual antenna array, the mutual coupling between elements can affect the measurement results and hence lead to inaccurate images. While a 3D full-wave simulation can account for the mutual coupling for a specific array, it could be computationally expensive for electrically large structures, and the scope of this work is more general. Nevertheless, this effect is expected to be more prominent at wider scanning angles, which is not necessarily the goal of every imaging application. Moreover, it does not affect the conclusions of this work.

REFERENCES

[1] D. M. Sheen, D. L. McMakin and T. E. Hall, "Three-dimensional millimeter-wave imaging for concealed weapon detection," in *IEEE Transactions on Microwave Theory and Techniques*, vol. 49, no. 9, pp. 1581-1592, Sept. 2001.

[2] R. Fukasawa, "Terahertz Imaging: Widespread Industrial Application in Non-destructive Inspection and Chemical Analysis," in *IEEE Transactions on Terahertz Science and Technology*, vol. 5, no. 6, pp. 1121-1127, Nov. 2015.

[3] Z. D. Taylor *et al.*, "THz Medical Imaging: in vivo Hydration Sensing," in *IEEE Transactions on Terahertz Science and Technology*, vol. 1, no. 1, pp. 201-219, Sept. 2011.

[4] S. k. Doddalla and G. C. Trichopoulos, "Non-Line of Sight Terahertz Imaging from a Single Viewpoint," *2018 IEEE/MTT-S International Microwave Symposium - IMS*, Philadelphia, PA, 2018, pp. 1527-1529.

[5] M. Aladsani, A. Alkhateeb and G. C. Trichopoulos, "Leveraging mmWave Imaging and Communications for Simultaneous Localization and Mapping," *ICASSP 2019 - 2019 IEEE International Conference on Acoustics, Speech and Signal Processing (ICASSP)*, Brighton, United Kingdom, 2019, pp. 4539-4543, doi: 10.1109/ICASSP.2019.8682741.

[6] K. B. Cooper, R. J. Dengler, N. Llombart, B. Thomas, G. Chattopadhyay and P. H. Siegel, "THz Imaging Radar for Standoff Personnel Screening," in *IEEE Transactions on Terahertz Science and Technology*, vol. 1, no. 1, pp. 169-182, Sept. 2011.

[7] R. Appleby and H. B. Wallace, "Standoff Detection of Weapons and Contraband in the 100 GHz to 1 THz Region," in *IEEE Transactions on Antennas and Propagation*, vol. 55, no. 11, pp. 2944-2956, Nov. 2007.

[8] C. A. Balanis, Antenna Theory: Analysis and Design, 4th edition. Hoboken, NJ, USA: John Wiley & Sons, 2016.

[9] Z. Hu, C. Wang and R. Han, "A 32-Unit 240-GHz Heterodyne Receiver Array in 65-nm CMOS With Array-Wide Phase Locking," in *IEEE Journal of Solid-State Circuits*, vol. 54, no. 5, pp. 1216-1227, May 2019, doi: 10.1109/JSSC.2019.2893231.

[10] R. L. Haupt, "Lowering the Sidelobe Level of a Two-Way Array Factor for an Array With Uniform Transmit and Uniform Receive Arrays," in *IEEE Transactions on Antennas and Propagation*, vol. 67, no. 6, pp. 4253-4256, June 2019, doi: 10.1109/TAP.2019.2905932.

[11] B. Baccouche et al., "Three-Dimensional Terahertz Imaging With Sparse Multistatic Line Arrays," in *IEEE Journal of Selected Topics in Quantum Electronics*, vol. 23, no. 4, pp. 1-11, July-Aug. 2017, Art no. 8501411.

[12] Z. Zhang and T. Buma, "Terahertz Impulse Imaging With Sparse Arrays and Adaptive Reconstruction," in *IEEE Journal of Selected Topics in Quantum Electronics*, vol. 17, no. 1, pp. 169-176, Jan.-Feb. 2011.

[13] L. Ding, S. Wu, X. Ding, P. Li and Y. Zhu, "Off-the-Grid Sparse Imaging by One-Dimensional Sparse MIMO Array," in *IEEE Sensors Journal*, vol. 18, no. 24, pp. 9993-10001, 15 Dec.15, 2018.

[14] WIPL-D 2D Solver v5.0, Belgrade, Serbia, WIPL-D d.o.o. Company. Available: https://wipl-d.com/products/wipl-d-2d-solver/.

[15] G. R. Lockwood and F. S. Foster, "Optimizing sparse two-dimensional transducer arrays using an effective aperture approach," *1994 Proceedings of IEEE Ultrasonics Symposium*, Cannes, France, 1994, pp. 1497-1501 vol.3.

[16] Y. Cui and G. C. Trichopoulos, "Seeing Around Obstacles with Terahertz Waves," arXiv preprint arXiv:2205.05066 (2022).

[17] M. Cetin, W. C. Karl, and D. A. Castanon, "Evaluation of a regularized SAR imaging technique based on recognition-oriented features," *Proceedings of the SPIE Conference on Algorithms for SAR Imagery VII*, vol. 4053, Orlando, FL, April 2000.

[18] D. Ao, Y. Li, C. Hu, and W. Tian, "Accurate Analysis of Target Characteristic in Bistatic SAR Images: A Dihedral Corner Reflectors Case," *Sensors*, vol. 18, no. 2, pp. 24, Dec. 2017.

[19] P. C. Theofanopoulos and G. C. Trichopoulos, "Toward Large-Scale Dynamically Reconfigurable Apertures Using Graphene," *2019 IEEE International Symposium on Antennas and Propagation and USNC-URSI Radio Science Meeting*, Atlanta, GA, USA, 2019, pp. 511-512.